Electronic Supplementary Information

Hybrids of iridium-cobalt phosphate as a highly efficient electrocatalyst for oxygen evolution reaction in neutral solution

Zhaoying Wang, Zheng Lin, and Peng Diao*

School of Material Science and Engineering, Beihang University, Beijing 100191, P.R. China.

* corresponding author, Email: pdiao@buaa.edu.cn

Experimental Section

Materials

Cobalt nitrate hexahydrate ($Co(NO_3)_2 \cdot 6H_2O$, 98.5%), iridium(III) chloride hydrate ($IrCl_3 \cdot xH_2O$, 99.9%), potassium dihydrogen phosphate (KH_2PO_4, 99.5%) and dipotassium hydrogen phosphate (K_2HPO_4, 99.5%) were purchased from Alfa Aesar Chemicals. Fluorine-doped tin oxide (FTO) substrates (8 Ω/square, transmittance of 80%) were purchased from Asahi Glass, Tokyo, Japan. All the chemicals used in this work were of analytical grade without further purification. All aqueous solutions in this work were prepared with deionized water (18 MΩ cm).

Preparation of Co-Pi, Ir-Pi, and IrCo-Pi on glass carbon electrode

The Co-Pi, Ir-Pi, and IrCo-Pi catalysts were prepared on a glass carbon (GC) or FTO electrode via a cyclic voltammetric deposition method, which was different from the potentiostatic deposition[1] usually employed to grow metal phosphate films on conductive substrates. In detail, CV deposition were performed on GC (or FTO) electrode (0.5 cm in diameter) for required cycles in the potential range from -0.04 V to 1.15 V (*vs.* SCE) at a scan rate of 0.05 V s^{-1} in 0.1 M potassium phosphate buffer solution (PBS, pH 7.0) containing different precursors. For the preparation of Co-Pi and Ir-Pi, the deposition solution contained 0.5 mM $Co(NO_3)_2$ and 0.5 mM $IrCl_3$, respectively. While for the growth of the IrCo-Pi hybrids, mixed solution of $Co(NO_3)_2$ and $IrCl_3$ was used with a constant Co^{2+} + Ir^{3+} concentration of 0.5 mM. The Ir-to-Co molar ratio ($R_{\text{Ir-to-Co}}$) of the deposition solution was varied to modulate the concentrations of Ir and Co in the obtained IrCo-Pi hybrid film. All electrochemical deposition were performed on a CHI660 electrochemical work station (CH Instruments Co., USA) in a three-electrode cell with a saturated calomel electrode (SCE) and a graphite rod as the reference and counter electrodes, respectively.

Material characterization

X-ray diffraction (XRD) patterns of Co-Pi, Ir-Pi and IrCo-Pi were recorded on a D/MAX-2500 Advance powder X-ray diffractometer (Rigaku Co., Japan) with Cu Kα radiation operating at 40 kV and 200 mA. Field-emission scanning electron microscopy (SEM) (JSM7500, JEOL Ltd., Japan) was employed to characterize the morphology and atomic composition of all samples, and the SEM images and energy dispersive spectra were obtained at an accelerating voltage of 3 kV and 20 kV, respectively. X-ray photoelectron spectroscopic (XPS) measurements were performed with an ESCALAB 250Xi instrument (ThermoFischer Co., USA) to characterize the surface composition and chemical states of Co-Pi, Ir-Pi and IrCo-Pi.

Electrochemical measurements

Electrochemical measurements were performed on a CHI660C workstation (CH Instruments Co., USA) in a three-electrode system, in which a freshly deposited IrCo-Pi (or Ir-Pi, or Co-PI), an SCE, and a graphite rod were employed as the working, the reference, and the counter electrodes, respectively. Unless specified, all the potentials in this work were reported with respect to the reversible hydrogen electrode (RHE) on the basis of the following equation:

$$E(\text{V } vs.\text{ RHE}) = E(\text{V } vs.\text{ SCE}) + 0.244 + 0.0592\text{pH} \quad (1)$$

where E(V *vs.* RHE) and E(V *vs.* SCE) are potentials with respect to RHE and SCE, respectively. Linear sweep voltammetry (LSV) was conducted in the potential range of 1.3 - 1.8 V (*vs.* RHE) in 0.1 M PBS (pH 7.0) with a scan rate of 5 mV s^{-1}. Electrochemical impedance spectroscopic (EIS) measurements were operated at 1.5 V (vs. RHE) with a frequency range from 106 to 0.01 Hz and an AC amplitude of 5 mV. The double layer capacitance of different samples were measured by CV at the potential sweep rate of 0.005, 0.010. 0.025, 0.05, 0.1, 0.2, 0.4, and 0.8 V s^{-1}. The real electrochemical surface areas (ECSA) of different samples were obtained according to the follow equation:[2]

$$\text{ECSA} = I_c/(v\ C_{dl}) \quad (2)$$

where I_c is the charging current, v is potential sweep rate, and C_{dl} is the normalized double layer capacitance of in μF cm^{-2}, which is estimated to be 230 μF cm^{-2}. All electrochemical data reported in this work was **not** iR compensated.

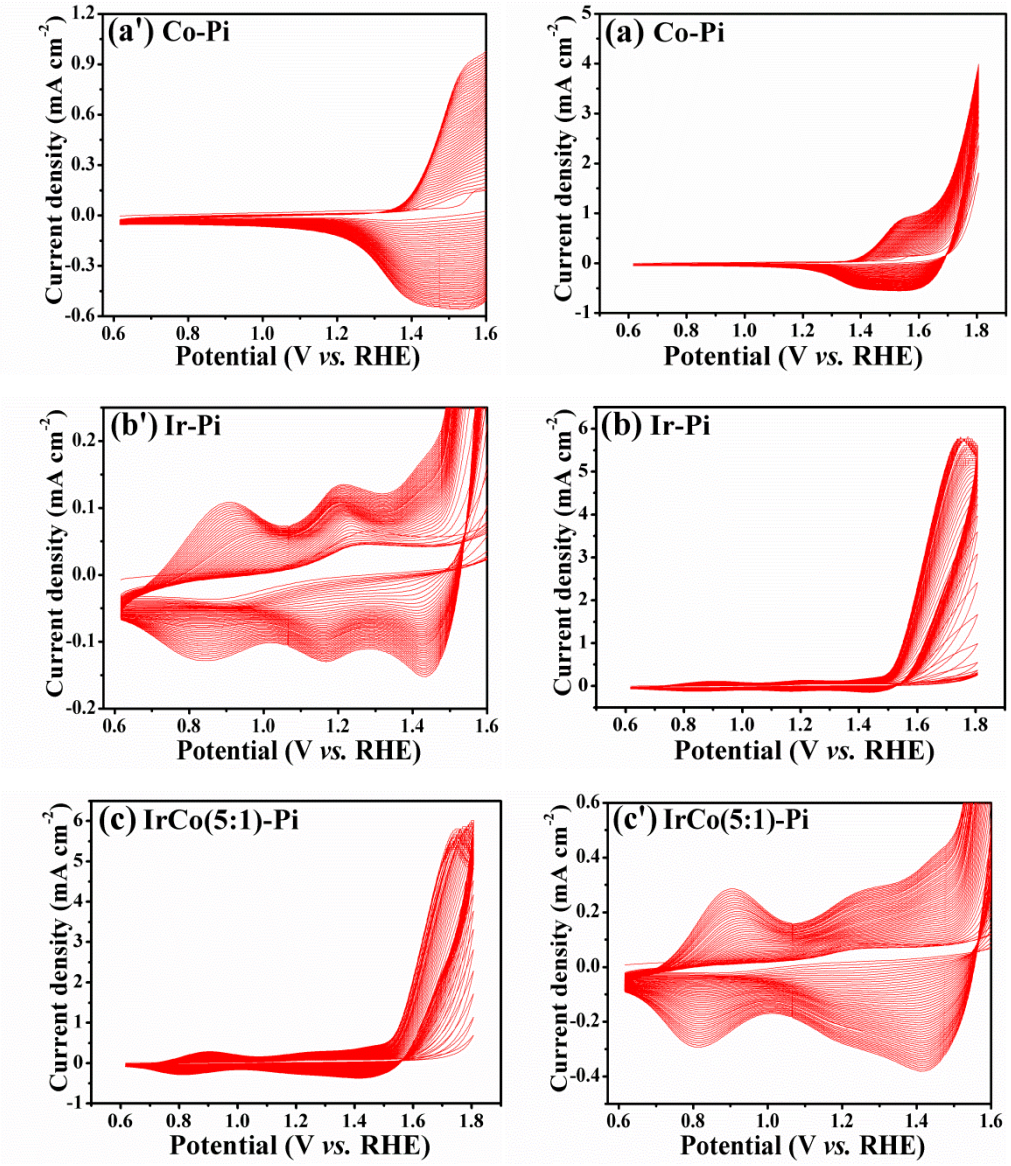

Figure S1. Cyclic voltammograms of the deposition process on GC electrodes in 0.1 M PBS (pH 7.0) containing (a) 0.5 mM Ir^{3+}; (b) 0.5 mM Co^{2+}; (c) 0.417 mM Ir^{3+} and 0.083 mM Co^{2+}. (a'),(b'), and (c') are the corresponding zoom-in images of (a), (b), and (c), respectively.

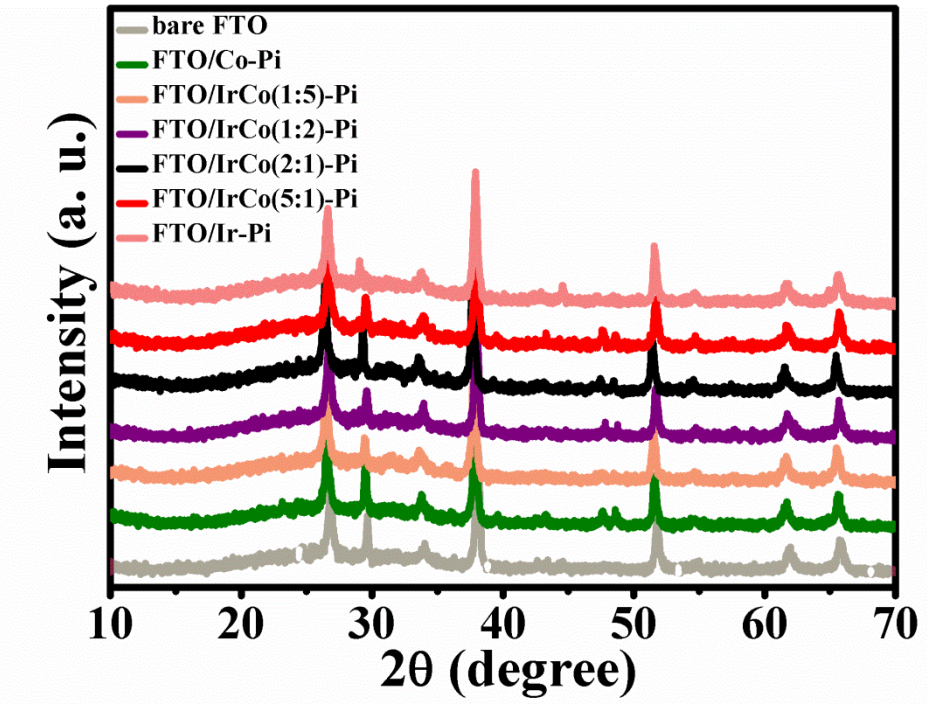

Figure S2. XRD patterns of bare FTO, FTO/Co-Pi, FTO/Ir-Pi, and FTO/IrCo-Pi with different $R_{\text{Ir-to-Co}}$.

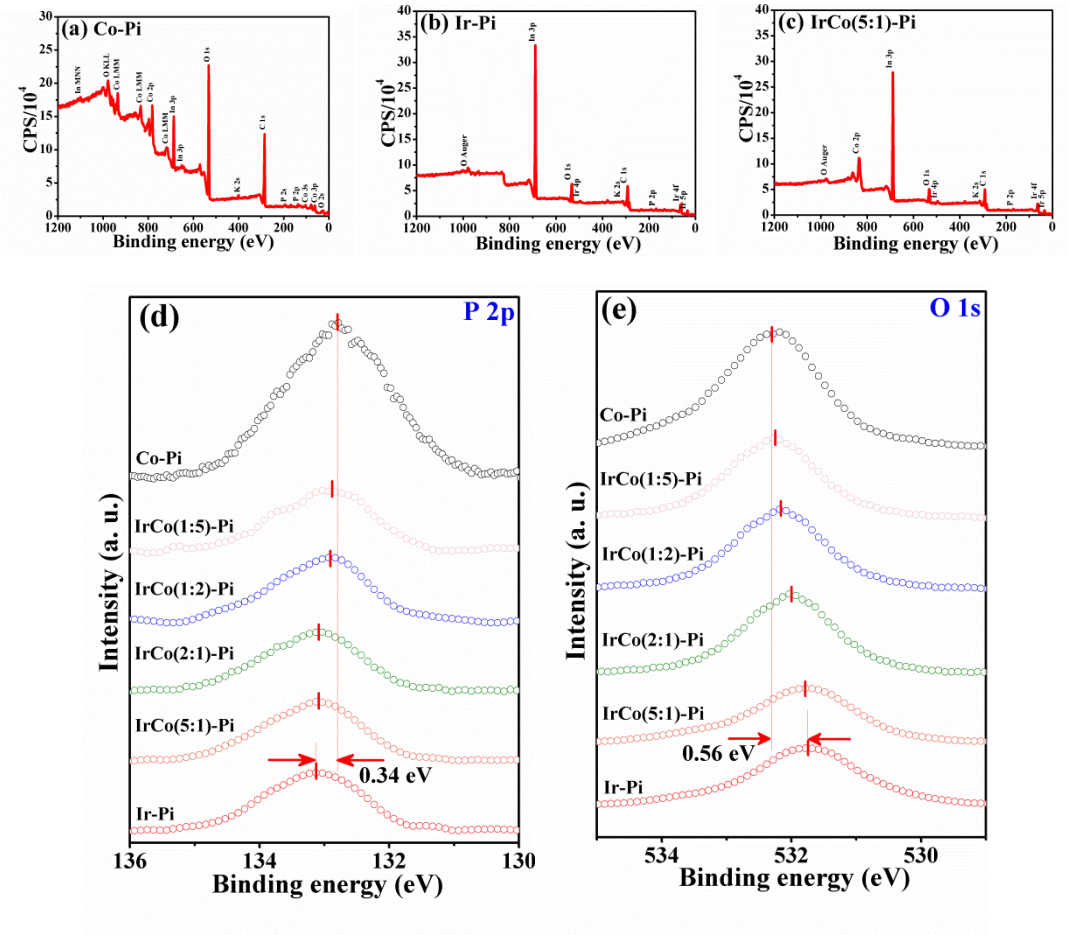

Figure S3. XPS survey spectra of (a) Co-Pi; (b) Ir-Pi; (c) IrCo(5:1)-Pi; high resolution XPS spectra of (d) P 2p; (e) O 1s in Co-Pi, Ir-Pi and IrCo-Pi.

The binding energy of P 2p peaks from Co-Pi and Ir-Pi are 132.79 and 133.13 eV, respectively. The P 2p signal originates from the phosphate ions.[1, 2] The binding energy of O 1s peaks from Co-Pi and Ir-Pi are 532.31 and 531.75 eV, respectively. The O 1s signal originates from the interaction between the metal and the absorbed oxygen species.[1, 3] In addition, the positive shift of O 1s peak position from Ir-Pi to IrCo-Pi and then to Co-Pi suggest partial electron transfer along Ir-O-Co bond.

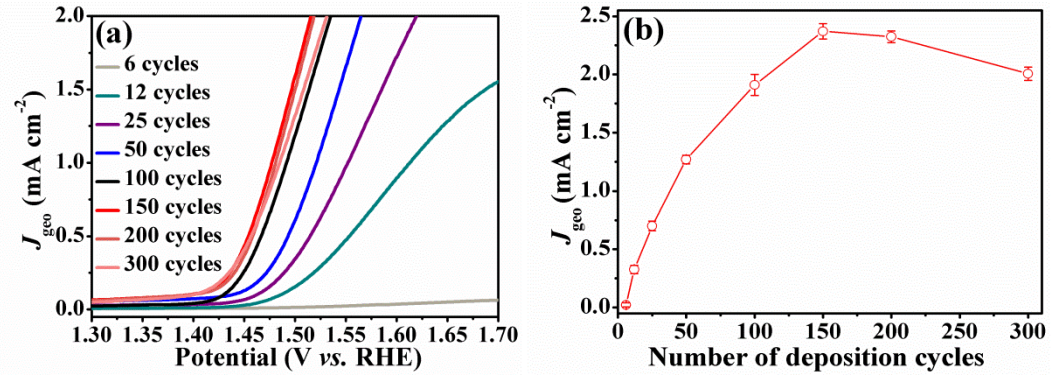

Figure S4. (a) Linear sweep voltammetry (LSV) curves of IrCo(5:1)-Pi prepared by CV co-deposition for different cycles; (b) The influence of IrCo(5:1)-Pi deposition cycle on the current density. The current density was obtained from (a) at an overpotential of 300 mV (1.53 V *vs.* RHE). The error bar in (b) comes from the variation of data obtained on different IrCo(5:1)-Pi samples prepared with the same deposition cycles.

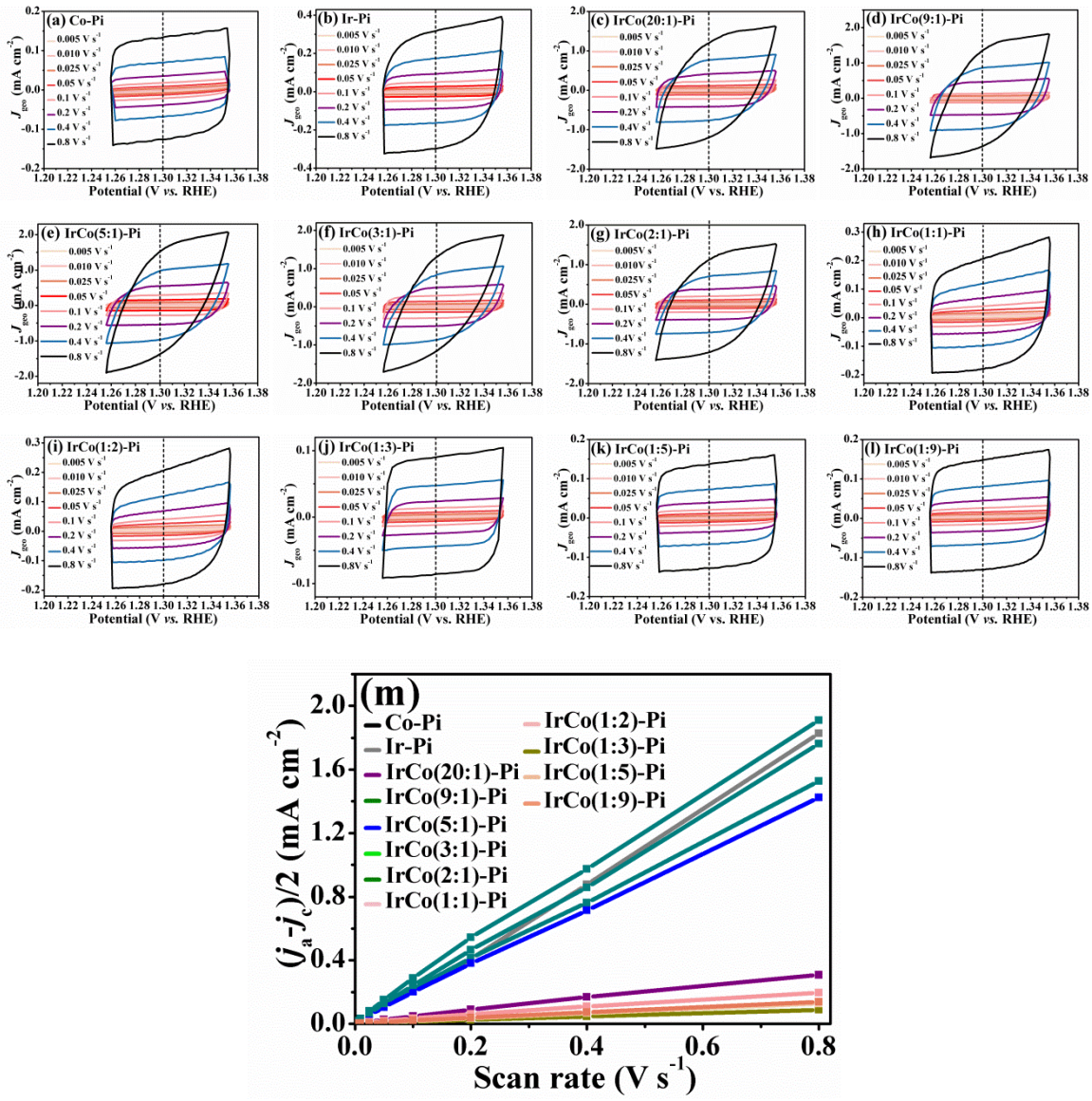

Figure S5. Cyclic voltammograms of (a) Co-Pi, (b) Ir-Pi, and (c)-(l) IrCo-Pi in an OER inert potential window at different scan rates, (m) The linear fitting extraction of the double-layer capacitance of all samples.

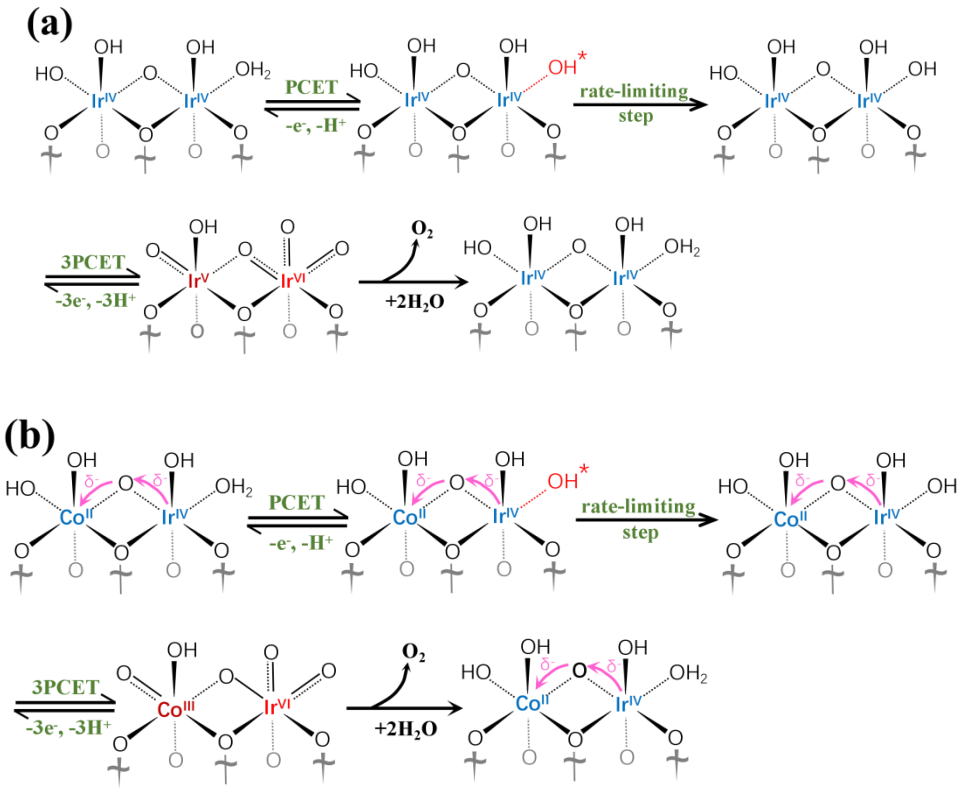

Scheme S1 Schematics of OER mechanisms on (a) Ir-Pi and (b) IrCo-Pi. Pink arrows show the partial electron transfer direction.

Table S1. Ir-to-Co molar ratio obtained by XPS on the surface of Co-Pi, Ir-Pi and IrCo-Pi catalysts.

Sample	**Ir-to-Co molar ratio in deposition solution for the preparation of catalyst**	**Ir-to-Co molar ratio on the surface of catalyst**
Ir-Pi	1:0	1:0
IrCo(5:1)-Pi	5:1	1:1.01
IrCo(2:1)-Pi	2:1	1:4.90
IrCo(1:2)-Pi	1:2	1:10.70
IrCo(1:5)-Pi	1:5	1:22.85
Co-Pi	0:1	0:1

Table S2. Comparison of electrocatalytic OER performance of the IrCo-Pi hybrids with different Ir-to-Co molar ratio ($R_{\text{Ir-to-Co}}$). All samples in this table were prepared by deposition for 50 cycles.

Ir-to-Co ratio	**η_{onest} (mV)**	**J_{geo} (mA cm^{-2}) @ η=300 mV**	**J_{ECSA} (mA cm^{-2}) @ η=300 mV**	**Tafel slope (mV dec^{-1})**	**ECSA (cm^2)**
Ir-Pi	285	0.40	0.17	57.1	0.32
IrCo(20:1)-Pi	282	0.49	0.19	60.8	1.61
IrCo(9:1)-Pi	248	1.17	0.29	50.9	1.87
IrCo(5:1)-Pi	246	1.21	0.32	58.6	2.07
IrCo(3:1)-Pi	256	0.99	0.24	57.3	1.83
IrCo(2:1)-Pi	259	0.87	0.18	57.0	1.32
IrCo(1:1)-Pi	287	0.33	0.15	61.0	0.20
IrCo(1:2)-Pi	305	0.21	0.13	82.9	0.15
IrCo(1:3)-Pi	393	0.09	0.12	131.1	0.09
IrCo(1:5)-Pi	408	0.10	0.11	133.9	0.14
IrCo(1:9)-Pi	402	0.11	0.12	148.9	0.15
Co-Pi	418	0.12	0.06	129.8	0.14

Table S3. Comparison of electrocatalytic OER performance of IrCo(5:1)-Pi with those reported on other transition metal phosphate catalysts.

Substrate	Catalyst	Electrolyte, pH	η_{onest} (mV)	Tafel slope (mV dec^{-1})	Reference
GC	Optimized IrCo(5:1)-Pi	0.1 M PBS, pH 7	208	51.4	This work
ITO	Co-Pi	0.1 M PBS, pH 7	280	60	[1]
CC	Co-Pi	0.1 M PBS, pH 7	340	60	[3]
CC	Ir-Pi	0.1 M PBS, pH 7	220	55	[3]
CP	Co-Ac-Pi	0.1 M PBS, pH 7	324	103	[4]
Ti mesh	Co-Pi	0.1 M PBS, pH 7	176	187	[5]
CC	Fe-Bi-Pi	0.1 M PBS, pH 7	322	94	[6]
FTO	$Mn_3(PO_4)_2$	0.5 M Na-Pi, pH 7	434	120	[7]
CC	Ni-Bi-Pi	0.1 M K-Bi, pH 9.2	220	139	[8]
GC	Co-Pi	0.1 M KOH, pH 13.2	346	83	[9]
GC	CoFe-Pi	0.1 M KOH, pH 13.2	252	33	[10]
GC	Mn-Pi	0.1 M KOH, pH 13.2	243	47	[11]
GC	CoFe-Pi	1 M KOH, pH 13.8	235	30	[12]
CP	FeCo-Pi	1 M KOH, pH 13.8	260	36	[13]
Ni foam	CoNi-Pi	1 M KOH, pH 13.8	163	59	[14]
NiFe foam	NiFe-Pi/NiFeP	1 M KOH, pH 13.8	188	57	[15]
GC	FeP/Fe-Pi	1 M KOH, pH 13.8	290	48	[16]
Ni foam	Fe-Pi	1 M KOH, pH 13.8	220	70	[17]
Ni foam	Fe_2PO_5	1 M KOH, pH 13.8	227	27	[18]
Ni foam	Fe-Pi	1 M KOH, pH 13.8	247	28	[19]
Ni foam	NiFe-Pi	1 M KOH, pH 13.8	237	37	[20]
Ni foam	$Ni_2P_2O_7$	1 M KOH, pH 13.8	211	52	[21]
GC	$Fe(OH)_3$/Ni-Pi	1 M KOH, pH 13.8	242	45	[22]
Ti foam	$Ni_{12}P_5/Ni_3(PO_4)_2$	1 M KOH, pH 13.8	268	52	[23]

Note: GC=glassy carbon electrode. ITO=indium-doped tin oxide. CC= carbon cloth. CP=carbon paper. FTO=fluorine-doped tin oxide.

Reference

1. M. W. Kanan and D. G. Nocera, Science, 2008, 321, 1072-1075.
2. A. J. Bard and L. R. Faulkner, Electrochemical Methods: Fundamentals and Applications, John Wiley & Sons, Inc, New York, 2nd edn., 2001.
3. A. Irshad and N. Munichandraiah, ACS Appl Mater Interfaces, 2015, 7, 15765-15776.
4. A. Irshad and N. Munichandraiah, Phys. Chem. Chem. Phys., 2014, 16, 5412-5422.
5. L. S. Xie, R. Zhang, L. Cui, D. N. Liu, S. Hao, Y. J. Ma, G. Du, A. M. Asiri and X. P. Sun, Angewandte Chemie-International Edition, 2017, 56, 1064-1068.
6. W. Wang, D. Liu, S. Hao, F. Qu, Y. Ma, G. Du, A. M. Asiri, Y. Yao and X. Sun, Inorganic Chemistry, 2017, 56, 3131-3135.
7. K. Jin, J. Park, J. Lee, K. D. Yang, G. K. Pradhan, U. Sim, D. Jeong, H. L. Jang, S. Park, D. Kim, N.-E. Sung, S. H. Kim, S. Han and K. T. Nam, Journal of the American Chemical Society, 2014, 136, 7435-7443.
8. M. Ma, D. Liu, S. Hao, R. Kong, G. Du, A. M. Asiri, Y. Yao and X. Sun, Inorganic Chemistry Frontiers, 2017, 4, 840-844.
9. J. B. Gerken, J. G. McAlpin, J. Y. C. Chen, M. L. Rigsby, W. H. Casey, R. D. Britt and S. S. Stahl, Journal of the American Chemical Society, 2011, 133, 14431-14442.
10. Y. Zhou and H. C. Zeng, Small, 2018, 14.
11. T. Zhang, S. Zhang, S. Cao, Q. Yao and J. Y. Lee, Chemistry of Materials, 2018, 30, 8270-8279.
12. D. Q. Yin, Z. Y. Jin, M. M. Liu, T. T. Gao, H. Y. Yuan and D. Xiao, Electrochimica Acta, 2018, 260, 420-429.
13. Z. J. Wang, M. Liu, J. Du, Y. Lin, S. X. Wei, X. Q. Lu and J. Zhang, Electrochimica Acta, 2018, 264, 244-250.
14. B. Liang, Y. Chen, J. He, C. Chen, W. Liu, Y. He, X. Liu, N. Zhang and V. A. L. Roy, Acs Applied Materials & Interfaces, 2018, 10, 3506-3514.
15. J. Li, W. Xu, D. Zhou, J. Luo, D. Zhang, P. Xu, L. Wei and D. Yuan, Journal of Materials Science, 2018, 53, 2077-2086.
16. J. Xu, D. Xiong, I. Amorim and L. Liu, ACS Applied Nano Materials, 2018, 1, 617-624.
17. P. T. Babar, A. C. Lokhande, H. J. Shim, M. G. Gang, B. S. Pawar, S. M. Pawar and J. H. Kim, Journal of Colloid and Interface Science, 2019, 534, 350-356.
18. Y. Wu, Y. Meng, J. Hou, S. Cao, Z. Gao, Z. Wu and L. Sun, Advanced Functional

Materials, 2018, 28, 1801397.

19. D. Zhong, L. Liu, D. Li, C. Wei, Q. Wang, G. Hao, Q. Zhao and J. Li, Journal of Materials Chemistry A, 2017, 5, 18627-18633.
20. Y. Li and C. Zhao, Chemistry of Materials, 2016, 28, 5659-5666.
21. S. J. Marje, P. K. Katkar, S. B. Kale, A. C. Lokhande, C. D. Lokhande and U. M. Patil, Journal of Alloys and Compounds, 2019, 779, 49-58.
22. W. Bian, Y. Huang, X. Xu, M. A. Ud Din, G. Xie and X. Wang, ACS Applied Materials & Interfaces, 2018, 10, 9407-9414.
23. J. Chang, Q. Lv, G. Li, J. Ge, C. Liu and W. Xing, Applied Catalysis B: Environmental, 2017, 204, 486-496.